Magnetic levitation of single cells

Naside Gozde Durmus[a,b,1], H. Cumhur Tekin[c,1], Sinan Guven[c], Kaushik Sridhar[c], Ahu Arslan Yildiz[c], Gizem Calibasi[c], Ionita Ghiran[d], Ronald W. Davis[a,b,e,2], Lars M. Steinmetz[b,e,2], and Utkan Demirci[c,2]

[a]Department of Biochemistry, School of Medicine, Stanford University, Stanford, CA 94304; [b]Stanford Genome Technology Center, Stanford University, Stanford, CA 94304; [c]Canary Center at Stanford for Cancer Early Detection, Radiology Department, School of Medicine, Stanford University, Stanford, CA 94304; [d]Department of Medicine, Beth Israel Deaconess Medical Center, Harvard Medical School, Boston, MA 02115; and [e]Department of Genetics, School of Medicine, Stanford University, Stanford, CA 94304

Several cellular events cause permanent or transient changes in inherent magnetic and density properties of cells. Characterizing these changes in cell populations is crucial to understand cellular heterogeneity in cancer, immune response, infectious diseases, drug resistance, and evolution. Although magnetic levitation has previously been used for macroscale objects, its use in life sciences has been hindered by the inability to levitate microscale objects and by the toxicity of metal salts previously applied for levitation. Here, we use magnetic levitation principles for biological characterization and monitoring of cells and cellular events. We demonstrate that each cell type (i.e., cancer, blood, bacteria, and yeast) has a characteristic levitation profile, which we distinguish at an unprecedented resolution of 1×10^{-4} g·mL^{-1}. We have identified unique differences in levitation and density blueprints between breast, esophageal, colorectal, and nonsmall cell lung cancer cell lines, as well as heterogeneity within these seemingly homogenous cell populations. Furthermore, we demonstrate that changes in cellular density and levitation profiles can be monitored in real time at single-cell resolution, allowing quantification of heterogeneous temporal responses of each cell to environmental stressors. These data establish density as a powerful biomarker for investigating living systems and their responses. Thereby, our method enables rapid, density-based imaging and profiling of single cells with intriguing applications, such as label-free identification and monitoring of heterogeneous biological changes under various physiological conditions, including antibiotic or cancer treatment in personalized medicine.

magnetic levitation | single cells | real-time monitoring | cell densitometry | cancer

Cells consist of micro- and nanoscale components and materials that have their own unique function along with fundamental magnetic and density signatures. For instance, organelles and the cytoplasm are encapsulated in a lipid bilayer membrane, which confines a living entity and gives it a unique density. Genetic mutations and functional changes at the proteomic level alter the cellular composition and thus might change inherent density signatures. Further biological changes during many physiological events, such as differentiation (1, 2), cell death (3, 4), aging (5), immune response (6, 7), or drug resistance (8) are accompanied by transient changes in cellular magnetic signatures, predominantly owing to the formation of intracellular paramagnetic reactive oxygen species. Characterizing these dramatic changes in fundamental cellular properties down to the individual cell level can reveal subpopulations in seemingly homogenous populations that cannot be seen using conventional assays, which average out or dilute changes in these cellular subsets (9).

A few methods exist to measure fundamental properties of cells, such as the density of cell populations. For example, ficoll gradient centrifugation separates cells in a liquid concentration gradient. However, this method can only estimate the "average" density of cell populations and thus does not provide accurate density measurements at the single-cell level. Furthermore, it is time-consuming and limited, because it requires a priori knowledge of cell density (10). These factors limit applications in life

sciences, where unbiased and precise measurements are needed, especially to understand cell-to-cell variability within homogenous or mixed cell populations (11, 12). In addition, exposure to concentrated solutions of substances used to construct the density gradient may inadvertently affect the density and viability of cells (13). A few methods have been developed to measure the density of single cells with high precision. Although nanomechanical resonators (14) allow measurement of cellular density, they require measurements in two separate fluids with known densities in a vacuum-packaged microcantilever that prevents real-time imaging and monitoring of dynamic cellular changes (10, 15). Dielectrophoretic field-flow fractionation has also been used to measure the density of different cell populations (i.e., cancer cells, erythrocytes, peripheral blood mononuclear cells); however, this method cannot measure the cell density at single-cell level (16). Alternatively, magnetic levitation (17–24) in large-scale instruments has been used to measure densities of mesoscale particles (>0.1 mm) (18) and to assemble macroscale objects (>1 mm) (17). However, the use of these systems for applications in life sciences is hindered by the inability to monitor microscale objects (<20 μm) and the use of concentrated metal salts that are toxic to living cells and biological systems.

Here, we demonstrate magnetic levitation of living cells and its application to detect minute differences in densities at the single-cell level, which serve as biophysical markers. First, we

Significance

Cells consist of micro- and nanoscale components and materials that contribute to their fundamental magnetic and density signatures. Previous studies have claimed that magnetic levitation can only be used to measure density signatures of nonliving materials. Here, we demonstrate that both eukaryotic and prokaryotic cells can be levitated and that each cell has a unique levitation profile. Furthermore, our levitation platform uniquely enables ultrasensitive density measurements, imaging, and profiling of cells in real-time at single-cell resolution. This method has broad applications, such as the label-free identification and monitoring of heterogeneous biological changes under various physiological conditions, including drug screening in personalized medicine.

levitated different cell types in our platform, MagDense, and measured their densities down to a resolution of 1×10^{-4} g·mL^{-1}. The platform allows real-time monitoring of single-cell densities and cellular responses under different stimuli (environmental stressor or drug treatment). Hence, MagDense is currently the only platform that can measure densities of single cells while performing label-free monitoring of single cells and heterogeneous cell populations (*SI Appendix*, Table S1).

Results and Discussion

Platform Design and Development. Our cell densitometry platform, MagDense, is composed of (*i*) two permanent magnets (50-mm length, 2-mm width, and 5-mm height) with the same poles facing each other, (*ii*) a channel (1-mm × 1-mm cross-section, 50-mm length and 0.2-mm wall thickness) between these magnets, and (*iii*) tilted side mirrors to measure the levitation height of cells inside the channel using a microscope (Fig. 1*A* and *SI Appendix*, Fig. S1). Cells spiked in a nonionic paramagnetic medium (i.e., Gadavist, Gd) move away from the larger magnetic induction site (**B**) (i.e., close vicinity to the magnets) to the lower magnetic field induction site (i.e., away from the magnets) (*SI Appendix*, Fig. S2) owing to the difference between the magnetic susceptibilities of cells and their surrounding medium ($\Delta\chi = \chi_c - \chi_m$)

(Fig. 1*B*). When they reach equilibrium, cells are levitated inside the medium at a position where the magnetic force (**F$_{mag}$**) equals the buoyancy force (**F$_b$**) (Fig. 1*B*). The equilibrium height of a cell along the channel height is calculated based on magnetic induction values B (25–27) and can be derived by solving the following equation:

$$\frac{\Delta\chi}{\mu_0}\left(B_x\frac{\partial B_z}{\partial x} + B_y\frac{\partial B_z}{\partial y} + B_z\frac{\partial B_z}{\partial z}\right) - \Delta\rho g = 0. \qquad [1]$$

The gravitational acceleration is represented by g, μ_0 defines the permeability of the free space, $\Delta\rho$ is the volumetric density difference between cell and paramagnetic medium (i.e., $\rho_c - \rho_m$), and x, y, and z are the coordinates of a cell. The magnetic susceptibilities of cells (28) are negligible compared with the magnetic susceptibility of the paramagnetic medium (29). Thus, cells are equilibrated at a unique levitation height mainly based on their density, independent of their volume. For instance, cells with the same density as the paramagnetic medium are equilibrated in the middle of the channel (i.e., $z = 0$) and cells with densities different from that of the medium are equilibrated above (if $\rho_c < \rho_m$) or below the middle of the channel (if $\rho_c > \rho_m$). In addition, cells are focused along the x
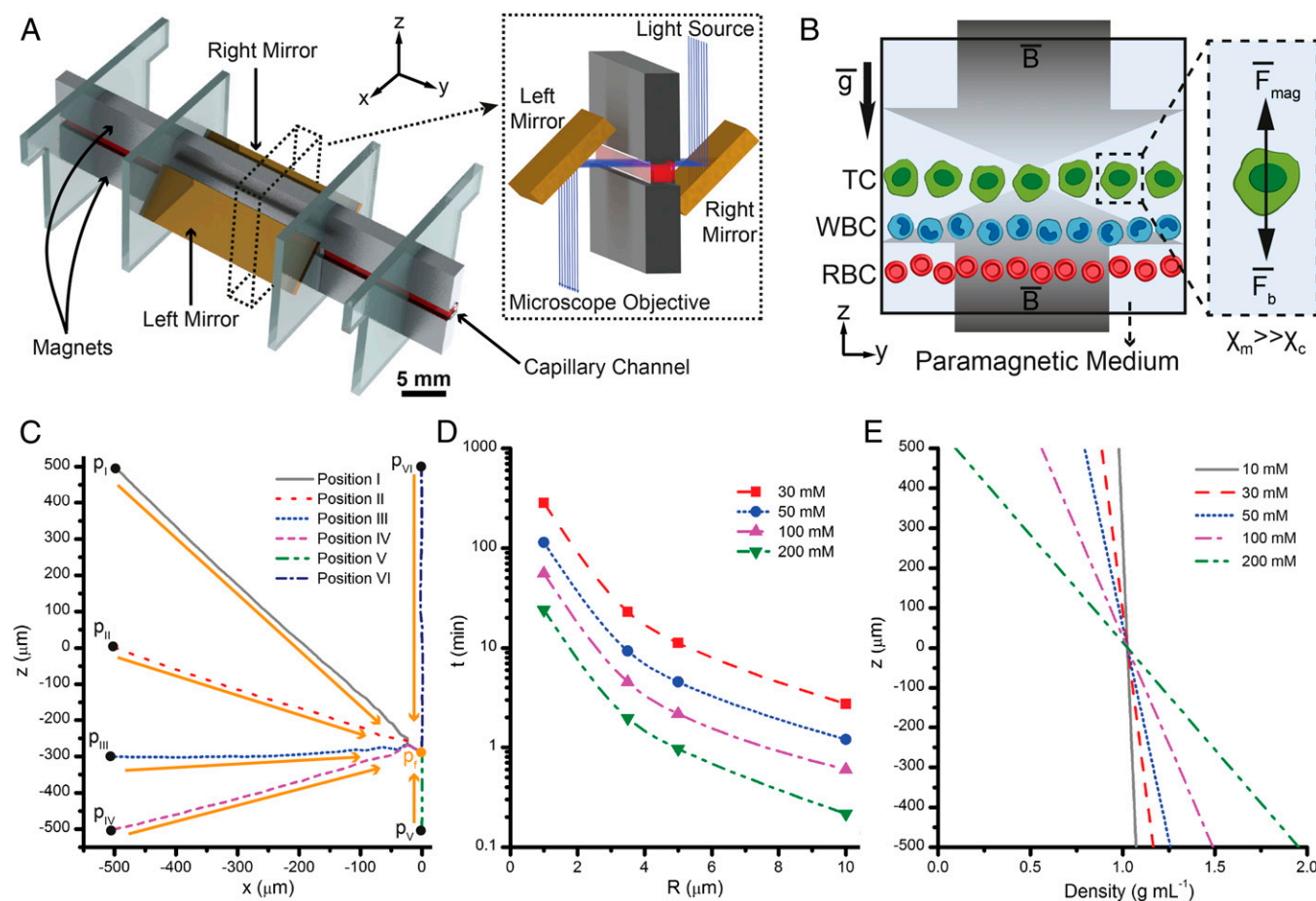

Fig. 1. Principles of the densitometry platform (i.e., MagDense cell density meter). (*A*) Illustration of the platform. PMMA pieces are used to hold the components of the platform (mirrors, neodymium magnets, and glass capillary channel) together. (*B*) Final equilibrium height of cells in MagDense. Owing to the magnetic induction (**B**) and gravity (**g**), cells are levitated in the channel and are focused in an equilibrium plane where magnetic forces (**F$_{mag}$**) and buoyancy forces (**F$_b$**) equilibrate each other. Magnetic susceptibility of the medium (χ_m) is chosen to be bigger than the cells' magnetic susceptibility (χ_c). Different cell types with different densities, such as cancer cells (TC), WBC, and RBC, are separated from each other. (*C*) Modeled motions of cells placed in six different initial positions (p_I–p_{VI}). RBC cell parameters are selected for these simulations. Over time, all cells are equilibrated at the same final position (p_f). In these simulations, 30 mM Gd solution is used. ($x = 0$ and $z = 0$ present the middle of the channel width and height, respectively). (*D*) Equilibrium time of cells. Different radiuses of cells are simulated in various paramagnetic medium concentrations. (*E*) Density curves of cells along the channel height for different simulated paramagnetic medium concentrations.

axis toward the middle of the channel (Fig. 1C), where the magnetic induction strength is lowest (*SI Appendix*, Fig. S2). As the paramagnetic solution concentration and/or cell radius increases, cells come to an equilibrium position more rapidly (Fig. 1D and *SI Appendix*, Fig. S3). By inducing a high magnetic induction gradient (i.e., 600 T m^{-1}) (*SI Appendix*, Fig. S2) using permanent magnets along the channel height, cell densities can be measured at a nontoxic paramagnetic concentration (i.e., lower than 100 mM) (*SI Appendix*, Fig. S4). Furthermore, densities of cells along the 1-mm channel height can be measured with a tunable resolution and range simply by changing the concentration of the paramagnetic medium (Fig. 1E). Various cell types with different sizes down to submicrometer level can be analyzed without changing the design of the platform (*SI Appendix*, Fig. S5).

We validated this platform using polyethylene beads (Fig. 2 and *SI Appendix*, Fig. S6). Beads spiked in fetal bovine serum (FBS) with 30 mM Gd were introduced into the levitation channel. In less than 5 min, several thousand beads levitated in different heights based on their density (Fig. 2A). The levitation height of beads can be altered using different Gd concentrations (i.e., 10 mM, 30 mM, and 50 mM) (Fig. 2B). Fitting the resulting plot of density versus levitation height to a liner curve provides a standard function to measure densities of cells and particles. The resolution can be tuned from 1×10^{-4} g·mL^{-1} to 5.5×10^{-4} g·mL^{-1} within a density range of 0.74–1.30 g·mL^{-1} by changing the Gd concentration from 10 mM to 50 mM (Fig. 2C and *SI Appendix*, Table S2). As expected, these experimental results matched with the theoretical simulations, allowing reference-free measurements. Further information on modeling and simulation results is provided in *Materials and Methods*.

Levitation-Based Density Profiling of Single Cells.

To assess our ability to characterize cells, we levitated and measured the densities of various mammalian cells (Fig. 3). Breast adenocarcinoma (MDA-MB-231), esophageal adenocarcinoma (JHEsoAD1), colorectal adenocarcinoma (HT29), colorectal carcinoma (HCT116), and nonsmall cell lung adenocarcinoma (HCC827) cell lines as well as different blood cells (i.e., white and red blood cells) were levitated in FBS containing 30 mM paramagnetic Gd solution. Within a few minutes, different cancer cell types were equilibrated at unique levitation heights, forming distinct cell-specific density bands (Fig. 3A). In addition, densities of several hundred cells were rapidly measured individually, producing a dot plot of densities as a function of cell size (Fig. 3B and *SI Appendix*, Fig. S7). In the literature, density distributions of red and white blood cells are reported to be between 1.080–1.120 g·mL^{-1} and 1.055–1.095 g·mL^{-1}, respectively (30, 31). As expected, the average density of red and white blood cells was measured as 1.109 and 1.088 g·mL^{-1} using our platform (*SI Appendix*, Table S3). The ability to distinguish rare circulating tumor cells (CTCs) from whole blood can further the understanding of cancer metastasis and enhance the monitoring and treatment of cancer patients. Notably, cancer cell populations showed signatures clearly distinguishable from those of white and red blood cells within the MagDense platform. Even colorectal cancer cells from different origins showed distinct density profiles; HCT116 and HT29 cells had a density of 1.063 ± 0.007 g·mL^{-1} and 1.084 ± 0.012 g·mL^{-1}, respectively. Furthermore, we observed heterogeneity within each seemingly homogenous cell population (*SI Appendix*, Table S3). Breast cancer is a heterogeneous disease with many biological features and clinical behaviors (32). In this respect, we observed that, among various cancer cell populations, the MDA-MB-231 cell line has the most
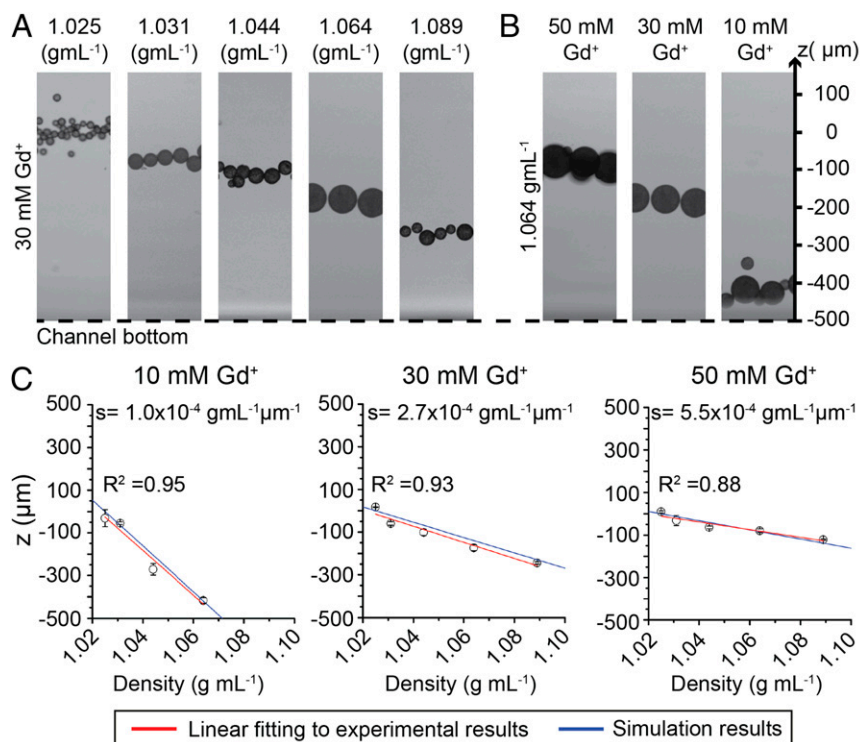

Fig. 2. Density measurement of polyethylene beads in the magnetic levitation platform. (A) Beads (10–100 μm in diameter) with different densities (1.025 g·mL^{-1}, 1.031 g·mL^{-1}, 1.044 g·mL^{-1}, 1.064 g·mL^{-1}, and 1.089 g·mL^{-1}) had distinct levitation heights in 30 mM Gd. (B) Beads with 1.064 g·mL^{-1} density had different levitation heights in different Gd concentrations (10 mM, 30 mM, and 50 mM). (C) The relationship between the bead density and levitation heights in 10 mM, 30 mM, and 50 mM Gd concentration, respectively. Data are plotted as mean of replicates with error bars (± SD). Linear fitting curve of the data points provides a standard function for measuring densities of particles/cells. The slope of each curve (s), which represents the amount of density change per micrometer levitation height, is presented for each figure. Expected density curves based on simulation results are also shown for each Gd concentration.
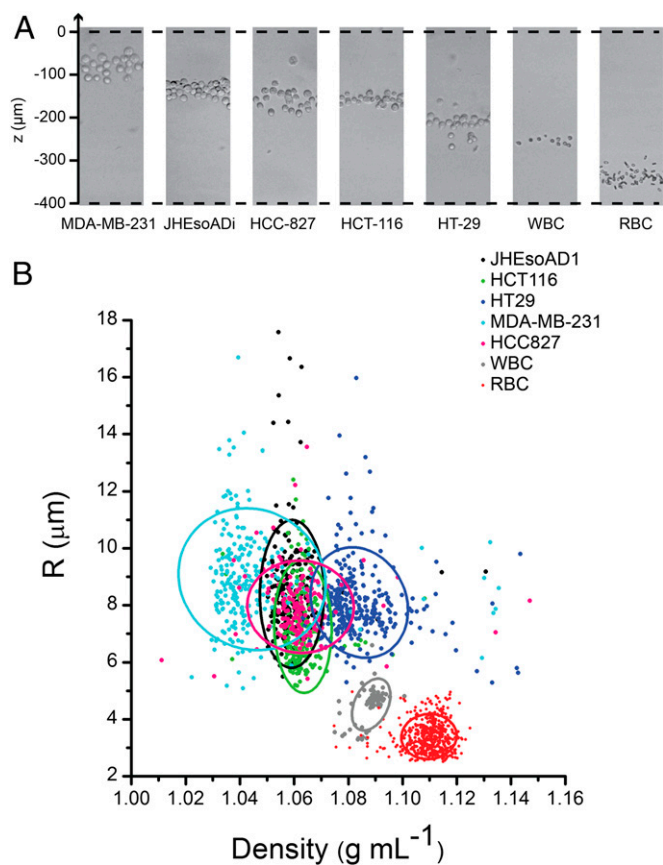
Fig. 3. Levitation-based density measurement of cells. (*A*) Distribution of cancer and blood cells in the MagDense along the channel (HCC827, non-small cell lung adenocarcinoma cells; HCT116, colorectal carcinoma cells; HT29, colorectal adenocarcinoma cells; JHesoAD1, esophageal adenocarcinoma cells; MDA-MB-231, breast adenocarcinoma cells). (*B*) Dot plot of cell density versus radius distribution of different cells. Principal component analysis was applied to present the correlation circles of each cell population. We observed that breast cancer cells had the lowest cell density, 1.044 ± 0.018 g·mL^{-1}, with a radius of 8.92 ± 1.64 µm, and RBC had the highest density, 1.109 ± 0.008 g·mL^{-1} with a radius of 3.55 ± 0.61 µm. The density and radius profiles of other cells were distributed as follows: (*i*) white blood cells with 1.088 ± 0.005 g·mL^{-1} and 4.52 ± 0.60 µm, (*ii*) esophageal cancer cells with 1.059 ± 0.008 g·mL^{-1} and 8.40 ± 1.71 µm, and (*iii*) lung cancer cells with 1.062 ± 0.013 g·mL^{-1} and 7.95 ± 1.07 µm.

heterogeneous cancer cell population with a density variance (σ^2) of 0.0003 (g·mL^{-1})^2. Thus, our levitation-based density profiling approach provides a simple method to investigate multiple cell types without using any labels or external energy sources.

Real-Time Monitoring of Cellular Response to Environmental Stressors. We investigated dynamic changes in cellular levitation and density signatures under environmental stress conditions (Fig. 4). While cell death occurs, cells change in size, surface-to-volume ratio, and density (33). Under neutral pH conditions, we observed that levitation heights and density profiles of human breast cancer cells are stable during 1 h of exposure. We, however, observed significant changes when these cells were exposed to acidic conditions over 1-h exposure (Fig. 4*A*). Using fluorescent markers (i.e., calcein and propidium iodide) as a measure of cell viability, we observed that cells turned from green to red as they sank toward the bottom of the channel, indicating a dying cell (Fig. 4*B* and Movie S1). We observed that changes in density of 5% preceded the onset of changes in fluorescence. Moreover, we quantified cell heterogeneous responses to the microenvironment in real time

(Fig. 4*C* and SI Appendix, Fig. S8). During acidic treatment in 30 mM Gd solution, we observed dynamic changes in levitation heights and cell densities, ranging from 1.05 g·mL^{-1} to 1.15 g·mL^{-1}. Dead cells also yielded a more heterogeneous density profile than live cells with a variance of 0.0007 (g·mL^{-1})^2 (SI Appendix, Fig. S9). Thus, characteristic cellular levitation and density profiles changed dynamically in response to variations in the environmental condition and each individual cell presented its response in a different manner and time scale.

Changes in Levitation and Density Profiles of Microorganisms After Drug Treatment. Another interesting application enabled by our platform is the levitation profiling and density measurement of microorganisms subjected to different drug treatments. During antibiotic treatment, bacterial cells undergo many biological changes that alter cellular composition. For instance, channels or ion pumps are created to excrete antibiotics. In addition, bacteria change their protein expression profiles and create antimicrobial destroying enzymes, which lead to changes in cell mass and density (34). Here, we rapidly detected significant changes in levitation and density profiles of *Escherichia coli* after various antibiotic treatments (Fig. 5*A*). Untreated *E. coli* cells had an average density of 1.139 ± 0.016 g·mL^{-1}, which is consistent with the reported values for bacteria (SI Appendix, Table S3) (35). However, ciprofloxacin, a fluoroquinolone antibiotic that inhibits DNA gyrase and cell division (36), killed 60% of the bacterial population (SI Appendix, Fig. S10). This led to the formation of a subpopulation at the 1.2–1.3 g·mL^{-1} density range, which is denser compared with the untreated controls. In addition, gentamicin, an aminoglycoside antibiotic that irreversibly binds to the 30S subunit of the ribosome and interrupts protein synthesis (37), killed 99% of the bacterial population (SI Appendix, Fig. S10) and increased the density of the population to 1.2–1.3 g·mL^{-1}. Thus, antibiotics with different mechanisms of action affect bacterial levitation and density profiles in a different manner.

We also applied our platform to yeast (*Saccharomyces cerevisiae*) (Fig. 5*B*). The density of the wild-type BY4743 strain from an asynchronous population was 1.119 ± 0.011 g·mL^{-1}, consistent with the values reported in the literature (SI Appendix, Table S3) (38, 39). We then treated wild-type yeast with 100 µM cantharidin or fluconazole. CRG1 gene expression provides resistance to cantharidin and, as expected, we did not observe significant changes in levitation and density profiles when comparing cantharidin-treated to untreated control cells (40). However, because the wild-type strain is sensitive to fluconazole (SI Appendix, Fig. S11), the levitation and density profiles significantly changed after overnight treatment. We also observed that upon drug treatment live and dead microorganisms have distinct density signatures (Fig. 5*C*). Hence, changes in cellular levitation height and density are correlated with the efficacy of a drug treatment. Drug resistance is a growing global healthcare problem and a significant challenge of our age (41, 42). There is significant need for point-of-care tools to distinguish resistant strains from nonresistant strains, especially for slow-growing species. Thus, this platform has the potential to rapidly test the efficacy of antimicrobial treatments and it can be used for antimicrobial susceptibility testing.

We have shown that our platform can characterize densities of both prokaryotic and eukaryotic cell types, including cancer and blood cells, as well as smaller cells, such as bacteria and yeast. Moreover, each cell has its own characteristic levitation and density profile that can be detected without using biomarkers, antibodies, or tags. The current platform enables single-cell density measurements of hundreds of cells within a few minutes using an automated, custom software. For various biological applications, analyses of higher numbers of cells in shorter time periods are required. For instance, flow cytometry methods can analyze 1,000–5,000 cells per second (43). Future generations of our technology can potentially continuously process cells in
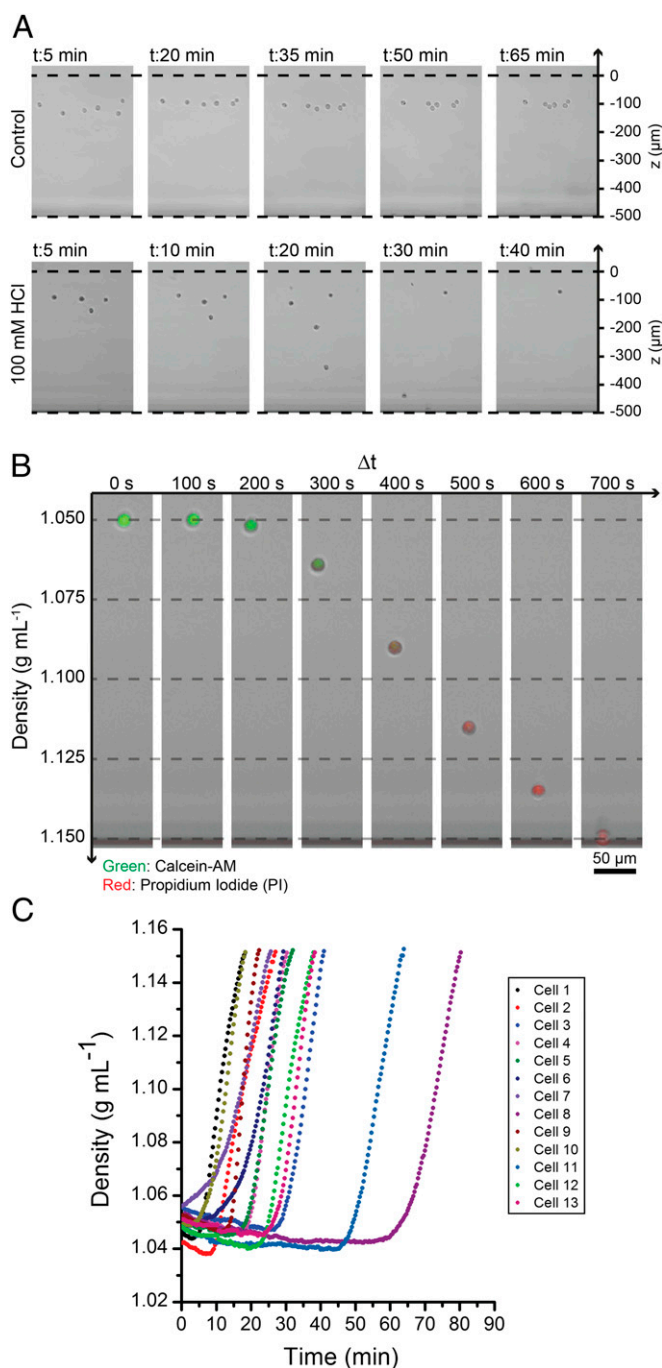
Fig. 4. Real-time density changes of single cells. (*A*) Micrographs of breast cancer cells in control (neutral pH) and acidic microenvironments (100 mM HCl). Cells in normal medium conditions maintain their levitation heights, whereas cells in the acidic environment sink to the bottom of the channel over time ($z = -500$ µm). (*B*) Real-time observation of a single cell in the acidic environment. Cell viability is also examined by calcein (green fluorescence) to detect live cells and PI (red fluorescence) to detect dead cells. Fluorescent and bright-field images were merged to compose the micrographs at different time points. As the cell was sinking through the bottom of the channel and increasing in density, its fluorescence profile was changing from green to red, indicating a dying cell. (*C*) Real-time density measurement of single cells in the acidic environment. Although the acidic treatment is applied to the cells at the same time, each cell behaves and responds differently. Heterogeneous changes in cellular density profiles can be detected in real time using the MagDense platform.

parallel channels, in which cells are flowed, levitated, and analyzed simultaneously. This would enable high-throughput analysis of thousands of cells and enable applications such as monitoring of CTCs. Moreover, cells at different levitation heights might be collected for downstream transcriptomic and proteomic analysis towards personalized and precision medicine. The simplicity, small size scale, and versatility of our platform design make the system compatible with mobile devices for telemedicine applications and offer an easy to setup and use system for biological or clinical laboratories. Future applications of this system, when implemented as an inexpensive, energy-free, label-free diagnostic device, might include utilizations in resource-constrained settings such as monitoring sickle cell disease (44).

Materials and Methods

Experimental Setup. MagDense consists of two N52-grade neodymium magnets (NdFeB) (50-mm length, 2-mm width, and 5-mm height), microcapillary channel (1-mm × 1-mm cross-section, 50-mm length, and 0.2-mm wall thickness) and mirrors (*SI Appendix*, Fig. S1). These parts were assembled using 1.5-mm-thick polymethyl methacrylate (PMMA) pieces that were cut with a laser system (VLS 2.30 Versa Laser) (45). Before each separate measurement, a microcapillary channel was plasma treated for 2 min at 100 W, 0.5 Torr (IoN 3 Tepla) and then placed between the magnets. Two mirrors were placed at 45° to image levitation heights using an inverted microscope (Zeiss Axio Observer Z1) under a 5× objective or 20× objective. The illumination of the microscope was aligned with respect to our platform mirror (i.e., left mirror shown in Fig. 1*A*, *Inset*).

Cell Culture. MDA-MB-231, HCT116, HT29, HCC827, and JHEsoAD1 cells were cultured in DMEM supplemented with 10% FBS and 100 units·mL^{-1} penicillin–streptomycin (Invitrogen Corp.). The cells were grown at 37 °C and 5% CO$_2$ in a humidified atmosphere. *E. coli* (DH5α strain) cells were hydrated and streaked for isolation on a Luria Bertani agar plate. Following growth, a single isolated colony was selected and inoculated in 3 mL of LB media. The bacteria culture was grown on an incubator shaker for 18 h at 37 °C, 250 rpm until it reached the stationary phase. The concentration of stock cultures was calculated as 10^8 cfu·mL^{-1}. Wild-type BY4743 yeast cells were grown in yeast extract peptone dextrose medium at 30 °C.

Sample Measurements. Cells and particles were spiked in FBS with various Gd concentrations (10 mM, 30 mM, 50 mM, and 100 mM). Thirty microliters of sample was pipetted into the microcapillaries and the channel was sealed with Critoseal. The samples were levitated for 30 min until they reached their equilibrium heights within the system. For bacteria, the samples were levitated for 2 h. Then, levitation heights and radiuses of cells were imaged and analyzed with in-house developed MATLAB code.

Modeling and Simulation Results. During levitation, magnetic force ($\mathbf{F_{mag}}$), buoyancy force ($\mathbf{F_b}$), and drag forces ($\mathbf{F_d}$) are induced on the cells:

$$\mathbf{F_{mag}} + \mathbf{F_b} + \mathbf{F_d} = 0. \qquad [2]$$

Cells are levitated in the channel with $\mathbf{F_{mag}}$ (27):

$$\mathbf{F_{mag}} = (\mathbf{m} \cdot \nabla)\mathbf{B}, \qquad [3]$$

where $\mathbf{B}$ is the magnetic induction, ∇ is the del operator, and $\mathbf{m}$ is the magnetic moment, which is calculated as

$$\mathbf{m} = \frac{V \Delta \chi}{\mu_0} \mathbf{B}, \qquad [4]$$

with V the volume of the cell, μ_0 the permeability of the free space (1.2566 × 10^{-6} kg·m·A^{-2}·s^{-2}) and $\Delta \chi$ the magnetic susceptibility difference between the cell and paramagnetic medium. $\mathbf{B}$ induced in the channel by opposing magnets is simulated using finite element method with COMSOL 4.0a (*SI Appendix*, Fig. S2). In these simulations, the residual magnetic induction (B_r) of magnets is assumed as 1.45 T according to the manufacturer data (K&J Magnetics).

During the levitation, cell gained velocity $\mathbf{v}$ and $\mathbf{F_d}$ is exerted on the cell. $\mathbf{F_d}$ is calculated for spherical object as follows (27):

$$\mathbf{F_d} = 6\pi R \eta f_D \mathbf{v}, \qquad [5]$$

where R is the radius of the cell, η is the dynamic viscosity of the paramagnetic medium, and f_D is the drag coefficient, which is equal to 1 when the cell is far away from the channel wall.
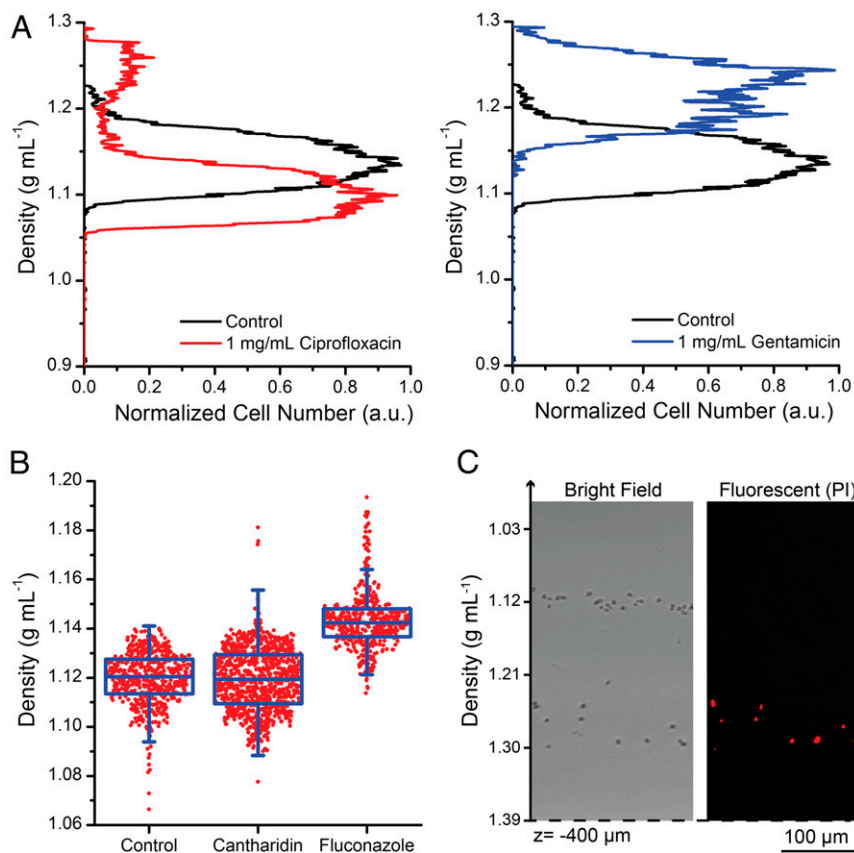
Fig. 5. Levitation profile and density measurement of microorganisms treated with drugs. (*A*) Density profiles of *E. coli* treated for 2 h with 1 mg·mL^{-1} ciprofloxacin and gentamicin, respectively. Control curves show *E. coli* density distribution without antibiotic treatment. Density measurements were conducted using 50 mM Gd. (*B*) Density dot plots of yeast cells treated with 100 μM cantharidin and fluconazole, compared with the untreated controls. After overnight drug treatment, cells were introduced into the platform with 50 mM Gd for density measurements. Corresponding OD measurements are provided in *SI Appendix*. (*C*) Micrographs of yeast cells treated with 1 mM fluconazole for 2 h in the levitation platform; 100 mM Gd was used to levitate the cells. Propidium iodide was used to identify dead cells.

F$_b$ is calculated as (25)

$$\mathbf{F_b} = V \Delta \rho \mathbf{g},\qquad[6]$$

where **g** is the gravitational acceleration (9.8 ms^{-2}), in z direction (Fig. 1) and ρ is the difference between the volumetric densities of the cell and the paramagnetic medium.

In the setup, cells are focused on the $x = 0$ plane where $B_x = 0$ with magnetic forces. However, the cell levitates in a certain height in z direction along $x = 0$ plane until magnetic and buoyancy forces come into balance:

$$\mathbf{F_{mag}} + \mathbf{F_b} = 0\qquad[7]$$

$$\frac{V\chi_m}{\mu_0}\left(B_x\frac{\partial B_z}{\partial x} + B_y\frac{\partial B_z}{\partial y} + B_z\frac{\partial B_z}{\partial z}\right) = V\Delta\rho g,\qquad[8]$$

where χ_m is the magnetic susceptibility of the paramagnetic medium, which is stronger than the cell's magnetic susceptibility [e.g., χ_c of RBC is around 4×10^{-6} (28)], and molar magnetic susceptibility of gadolinium-based paramagnetic solutions is 3.2×10^{-4} M^{-1} (29). As derived from Eq. **8**, cell radius (or V) does not affect the levitation height.

Cell motions in the setup are simulated using above equations in a custom-coded MATLAB program integrated with the **B** values calculated in COMSOL (*SI Appendix*, Fig. S2). RBC parameters are chosen in these simulations, where R is 3.5 μm and density of cell (ρ_c) is 1.1 g·mL^{-1} (46). For modeling, medium density (ρ_m) and viscosity (η) were chosen as 1.025 g·mL^{-1} and 1.105 cP (47), respectively. As shown in Fig. 1*C*, cells starting in different positions ended at the same final point along $x = 0$.

The longest cell trajectory path, which is p$_I$ to p$_f$ in Fig. 1*C*, is chosen to calculate the necessary equilibrium time of cells with different radiuses (Fig. 1*D*). As the paramagnetic solution concentration and/or radius of the cell increases, cells come to the equilibrium position more rapidly. For instance,

at 30 mM Gd concentration, cells with 3.5-μm radius (i.e., similar to RBC) are equilibrated in less than 30 min, whereas cells with 10-μm radius (i.e., similar to cancer cells) are equilibrated in less than 5 min. These simulation results also match with the experimental results presented in *SI Appendix*, Fig. S3.

Density profile along the channel is also simulated using different Gd concentrations (Fig. 1*E*). Using lower Gd concentrations increases the resolution of the density measurement. At the same time, it decreases the density range. All of the curves intersect at the middle of the channel ($z = 0$), where cells with the same density as the medium equilibrate. The density curves coming from simulation results show perfect correlation with the experimental results presented in *SI Appendix*, Fig. S5.

Thermal energy (E_T) can be effective on the cell, so Brownian motion can prevent the cell from levitating in the system. E_T is calculated as (48)

$$E_T = kT,\qquad[9]$$

where k is the Boltzmann constant ($1.3806488 \times 10^{-23}$ m2·kg-2·K^{-1}) and T is the temperature of the medium. To levitate cells, E_T should be lower than the sum of the kinetic energy (E_k) induced by magnetism, and the potential energy (E_p) induced by buoyancy. As shown in *SI Appendix*, Fig. S5, a wide range of cellular radius sizes, down to the submicrometer level, can be levitated using a 30 mM Gd concentration. To increase this radius range further, E_k can be increased using higher Gd concentrations. Bacteria and yeast can also be levitated using our setup (Fig. 5), which enables analysis of different types of cells and organisms without changing the platform design.

System Calibration with Polyethylene Beads. Fluorescent polyethylene beads (Cospheric LLC) (10–100 μm in size) with different densities (1.025 ± 0.007 g·mL^{-1}, 1.030 ± 0.007 g·mL^{-1}, 1.044 ± 0.007 g·mL^{-1}, 1.064 ± 0.007 g·mL^{-1}, and 1.089 ± 0.007 g·mL^{-1}) were suspended in FBS with various magnetic susceptibilities (10 mM, 30 mM, and 50 mM paramagnetic Gd solution). Then, the beads

Durmus et al.

were loaded into the microcapillaries and levitated (*SI Appendix*, Figs. S5 and S6). Fitting the resulting plot of density (grams per milliliter) versus levitation height (micrometers) to a linear curve provided a standard function to measure densities. Based on these curves, resolution and dynamic range of density measurements were calculated for different Gd concentrations (*SI Appendix*, Table S2).

Levitation of RBC. Blood samples from healthy donors were obtained from Stanford University Blood Center. Whole blood samples were diluted at a 1:100,000 ratio in FBS in 30 mM Gd.

Levitation of WBC. Whole blood was mixed with RBC lysis buffer at a 1:10 ratio. After 10 min of incubation, RBC were lysed and the blood sample was suspended at $200 \times g$ for 3 min. The resulting WBC pellet was resuspended in FBS in 30 mM Gd.

Levitation of Cancer Cells. MDA-MB-231, HCT116, HT29, JHEsoAD1, and HCC827 cells were centrifuged at $200 \times g$ for 3 min at room temperature. Then, culture medium was removed and cells were resuspended in FBS with 30 mM Gd. With respect to the measurements, cellular density versus radius distribution profile of cancer cells and also blood cells are presented in Fig. 3*B* and *SI Appendix*, Fig. S7. During magnetic levitation, cells can come close to each other and start to form aggregates, where cell–cell interactions could change the cellular morphology under long culture conditions (>2 d) (49). However, we do not expect to see this effect during these experiments because diluted cell samples and shorter levitation times were used.

Levitation of Bacteria and Antibiotic Treatments. Overnight cultures of *E. coli* cells (DH5α strain) were diluted at a 1:10 ratio. Then, the resulting cell solutions were treated with different classes of antibiotics: 1 mg/mL of ciprofloxacin (fluoroquinolone antibiotic) and gentamicin (aminoglycoside antibiotic), respectively. After 2 h of antibiotic treatment, cells were levitated in 50 mM Gd, covering the *E. coli* density range [i.e., 1.06–1.19 g·mL^{-1} (35)]. Corresponding OD graphs and levitation micrographs are presented in *SI Appendix*, Fig. S10.

Levitation of Yeast Cells and Drug Treatment. Overnight cultures of the *S. cerevisiae* strain BY4743 were diluted at a 1:100 ratio. Then, the resulting cell solutions were treated with 100 μM cantharidin or fluconazole. Untreated

cultures were used as controls. After overnight treatment, cells were suspended at $1,500 \times g$ for 5 min at room temperature. Then, cell media was removed and cells were resuspended in PBS with 50 mM Gd. Levitation micrographs and OD graphs are presented in *SI Appendix*, Fig. S11.

Real-Time Experiments. MDA-MB-231 cells were suspended at $200 \times g$ for 3 min. Then, the cell pellet was resuspended in 10 mM calcein in PBS. Cells were stained for 20 min at 37 °C. After staining, cells were suspended at $200 \times g$ for 3 min and resuspended in FBS with 30 mM Gd, propidium iodide (PI), and 100 mM HCl solution. Then, cells were levitated for 90 min and imaged every 20 s (Movie S1). Cellular positions were analyzed using a MATLAB program developed in-house to monitor cellular trajectories (*SI Appendix*, Fig. S8). Cells that were resuspended in FBS with 30 mM Gd and PI were levitated as controls. To measure the final density of breast cancer cells treated with 100 mM HCl, the same experiment was repeated in 100 mM Gd spiked in FBS (*SI Appendix*, Fig. S9). The viability assay was also conducted for the control and 100 mM HCl-treated cells without using the densitometry platform and Gd (*SI Appendix*, Fig. S12).

Long-Term Culture of Cells in Paramagnetic Medium. JHEsoAD1 cells were used for viability experiments (*SI Appendix*, Fig. S4). They were cultivated in DMEM supplemented with 10% FBS and penicillin/streptomycin (0.1 mg/mL) in a humidified incubator at 37 °C and 5% CO_2. The cells were seeded at a starting concentration of 25×10^3 cells/mL in a 48-well plate. The cells were exposed to different concentrations of Gd solution (0, 30, 50, and 100 mM). Culture medium was changed every 3 d. During each medium change, a fresh Gd solution was added. Live/dead assay was conducted using calcein/ethidium homodimer mixture to observe the viability of cells exposed to Gd during culturing. The cells were stained for 20 min, washed with PBS, and imaged under the fluorescence microscope. Cell viability was calculated from fluorescence images using ImageJ software. Proliferation profiles were observed using the cell counting method. Four different batches of cells were used on days 0, 1, 3, and 5 for the calculation of cell numbers.

1. Meacham CE, Morrison SJ (2013) Tumour heterogeneity and cancer cell plasticity. *Nature* 501(7467):328–337.
2. Maric D, Maric I, Barker JL (1998) Buoyant density gradient fractionation and flow cytometric analysis of embryonic rat cortical neurons and progenitor cells. *Methods* 16(3):247–259.
3. Martin SJ, Bradley JG, Cotter TG (1990) HL-60 cells induced to differentiate towards neutrophils subsequently die via apoptosis. *Clin Exp Immunol* 79(3):448–453.
4. Wyllie AH, Morris RG (1982) Hormone-induced cell death. Purification ad properties of thymocytes undergoing apoptosis after glucocorticoid treatment. *Am J Pathol* 109(1):78–87.
5. Storz P (2006) Reactive oxygen species-mediated mitochondria-to-nucleus signaling: A key to aging and radical-caused diseases. *Sci STKE* 2006(332):re3.
6. Satija R, Shalek AK (2014) Heterogeneity in immune responses: From populations to single cells. *Trends Immunol* 35(5):219–229.
7. Bumann D (2015) Heterogeneous host-pathogen encounters: Act locally, think globally. *Cell Host Microbe* 17(1):13–19.
8. Lee MC, et al. (2014) Single-cell analyses of transcriptional heterogeneity during drug tolerance transition in cancer cells by RNA sequencing. *Proc Natl Acad Sci USA* 111(44): E4726–E4735.
9. Altschuler SJ, Wu LF (2010) Cellular heterogeneity: Do differences make a difference? *Cell* 141(4):559–563.
10. Grover WH, et al. (2011) Measuring single-cell density. *Proc Natl Acad Sci USA* 108(27): 10992–10996.
11. Brennecke P, et al. (2013) Accounting for technical noise in single-cell RNA-seq experiments. *Nat Methods* 10(11):1093–1095.
12. Almendro V, Marusyk A, Polyak K (2013) Cellular heterogeneity and molecular evolution in cancer. *Annu Rev Pathol* 8:277–302.
13. Sharpe PT (1988) *Methods of Cell Separation*, Laboratory Techniques in Biochemistry and Molecular Biology, eds Burdon RH, van Knippenberg PH (Elsevier, Amsterdam), Vol 18.
14. Burg TP, et al. (2007) Weighing of biomolecules, single cells and single nanoparticles in fluid. *Nature* 446(7139):1066–1069.
15. Bryan AK, et al. (2014) Measuring single cell mass, volume, and density with dual suspended microchannel resonators. *Lab Chip* 14(3):569–576.
16. Shim S, Gascoyne P, Noshari J, Hale KS (2011) Dynamic physical properties of dissociated tumor cells revealed by dielectrophoretic field-flow fractionation. *Integr Biol (Camb)* 3(8):850–862.
17. Subramaniam AB, et al. (2014) Noncontact orientation of objects in three-dimensional space using magnetic levitation. *Proc Natl Acad Sci USA* 111(36):12980–12985.
18. Mirica KA, Ilievski F, Ellerbee AK, Shevkoplyas SS, Whitesides GM (2011) Using magnetic levitation for three dimensional self-assembly. *Adv Mater* 23(36):4134–4140.
19. Mirica KA, Phillips ST, Mace CR, Whitesides GM (2010) Magnetic levitation in the analysis of foods and water. *J Agric Food Chem* 58(11):6565–6569.
20. Bwambok DK, et al. (2013) Paramagnetic ionic liquids for measurements of density using magnetic levitation. *Anal Chem* 85(17):8442–8447.
21. Tasoglu S, et al. (2013) Paramagnetic levitational assembly of hydrogels. *Adv Mater* 25(8):1137–1143, 1081.
22. Lockett MR, Mirica KA, Mace CR, Blackledge RD, Whitesides GM (2013) Analyzing forensic evidence based on density with magnetic levitation. *J Forensic Sci* 58(1):40–45.
23. Tasoglu S, et al. (2014) Guided and magnetic self-assembly of tunable magnetoceptive gels. *Nat Commun* 5:4702.
24. Atkinson MBJ, et al. (2013) Using magnetic levitation to separate mixtures of crystal polymorphs. *Angew Chem Int Ed Engl* 52(39):10208–10211.
25. Gijs MA, Lacharme F, Lehmann U (2010) Microfluidic applications of magnetic particles for biological analysis and catalysis. *Chem Rev* 110(3):1518–1563.
26. Shevkoplyas SS, Siegel AC, Westervelt RM, Prentiss MG, Whitesides GM (2007) The force acting on a superparamagnetic bead due to an applied magnetic field. *Lab Chip* 7(10):1294–1302.
27. Tekin HC, Cornaglia M, Gijs MA (2013) Attomolar protein detection using a magnetic bead surface coverage assay. *Lab Chip* 13(6):1053–1059.
28. Inglis DW, Riehn R, Sturm JC, Austin RH (2006) Microfluidic high gradient magnetic cell separation. *J Appl Phys* 99(8):08K101.
29. van Osch MJP, Vonken EJPA, Viergever MA, van der Grond J, Bakker CJG (2003) Measuring the arterial input function with gradient echo sequences. *Magn Reson Med* 49(6):1067–1076.
30. Prall YG, Gambhir KK, Ampy FR (1998) Acetylcholinesterase: An enzymatic marker of human red blood cell aging. *Life Sci* 63(3):177–184.
31. Zucker RM, Cassen B (1969) The separation of normal human leukocytes by density and classification by size. *Blood* 34(5):591–600.
32. Weigelt B, Geyer FC, Reis-Filho JS (2010) Histological types of breast cancer: how special are they? *Mol Oncol* 4(3):192–208.
33. Bortner CD, Cidlowski JA (2002) Apoptotic volume decrease and the incredible shrinking cell. *Cell Death Differ* 9(12):1307–1310.
34. Knudsen SM, von Muhlen MG, Schauer DB, Manalis SR (2009) Determination of bacterial antibiotic resistance based on osmotic shock response. *Anal Chem* 81(16): 7087–7090.

Durmus et al.

35. Poole RK (1977) Fluctuations in buoyant density during the cell cycle of Escherichia coli K12: Significance for the preparation of synchronous cultures by age selection. *J Gen Microbiol* 98(1):177–186.

36. Hawkey PM (2003) Mechanisms of quinolone action and microbial response. *J Antimicrob Chemother* 51(Suppl 1):29–35.

37. Davis BD (1987) Mechanism of bactericidal action of aminoglycosides. *Microbiol Rev* 51(3):341–350.

38. Allen C, et al. (2006) Isolation of quiescent and nonquiescent cells from yeast stationary-phase cultures. *J Cell Biol* 174(1):89–100.

39. Bryan AK, Goranov A, Amon A, Manalis SR (2010) Measurement of mass, density, and volume during the cell cycle of yeast. *Proc Natl Acad Sci USA* 107(3):999–1004.

40. Hoon S, et al. (2008) An integrated platform of genomic assays reveals small-molecule bioactivities. *Nat Chem Biol* 4(8):498–506.

41. Durmus NG, Taylor EN, Kummer KM, Webster TJ (2013) Enhanced efficacy of superparamagnetic iron oxide nanoparticles against antibiotic-resistant biofilms in the presence of metabolites. *Adv Mater* 25(40):5706–5713.

42. Durmus NG, Webster TJ (2013) Eradicating antibiotic-resistant biofilms with silver-conjugated superparamagnetic iron oxide nanoparticles. *Adv Healthc Mater* 2(1):165–171.

43. Basiji DA, Ortyn WE, Liang L, Venkatachalam V, Morrissey P (2007) Cellular image analysis and imaging by flow cytometry. *Clin Lab Med* 27(3):653–670, viii.

44. Bartolucci P, Brugnara C, Teixeira-Pinto A (2012) Erythrocyte density in sickle cell syndromes is associated with specific clinical manifestations and hemolysis. *Blood* 120(15):3136–3141, and erratum (2014) 123(12):1972.

45. Tasoglu S, et al. (2015) Levitational image cytometry with temporal resolution. *Adv Mater*, 10.1002/adma.201405660.

46. Rhoades R, Bell DR (2013) *Medical Physiology: Principles for Clinical Medicine* (Lippincott Williams & Wilkins, Philadelphia), 4th Ed.

47. Cakmak O, et al. (2013) Microcantilever based disposable viscosity sensor for serum and blood plasma measurements. *Methods* 63(3):225–232.

48. Bruus H (2008) *Theoretical Microfluidics* (Oxford Univ Press, Oxford).

49. Sazonova OV, et al. (2011) Cell-cell interactions mediate the response of vascular smooth muscle cells to substrate stiffness. *Biophys J* 101(3):622–630.

Durmus et al.